# SUBSONIC HIGH-LIFT FLIGHT RESEARCH ON THE NASA TRANSPORT SYSTEM RESEARCH VEHICLE (TSRV)

Long P. Yip\*
NASA Langley Research Center
Hampton, Virginia

Paul M.H.W. Vijgen\*\*
High Technology Corporation
Hampton, Virginia

Jay D. Hardin† Lockheed Engineering and Sciences Company Hampton, Virginia

> C. P. van Dam†† University of California, Davis Davis, California

### Abstract

Flight tests are being conducted on the Transport Systems Research Vehicle (B737-100 aircraft) at the NASA Langley Research Center as part of a multiphased research program to obtain detailed flow characteristics on a multi-element, high-lift flap system. Recent test results obtained for a full-chord wing section including the slat, main-wing, and flap elements are presented. In addition, program status and future plans are discussed.

Pressure distributions were obtained using pressure belts over the slat, main-wing, and flap elements at one spanwise station. Test conditions included a range of flap deflections, chord Reynolds numbers (10 to 21 million), and Mach numbers (0.16 to 0.40). In addition to the pressure distributions, Preston-tube measurements on the slat upper surface indicated relaminarization of turbulent flows which were introduced by the pressure belt on the slat leading-edge Comparisons of the in-flight pressure measurements with predictions from a two-dimensional, viscous multi-element method modified by simplesweep theory showed reasonable agreement; however, the overprediction of pressures on the flap elements shows a need for better modeling of confluent boundary layers and inclusion of three-dimensional effects.

*Research En	gineer,	Flight	Research	Branch,	Flight
Applications D	ivision. S	Senior N	Aember Al	AA.	J
**Research So	cientist a	t Lami	nar Flow	Control	Project
Office, NASA I	Langley. N	<b>Member</b>	AIAA.		•
†Research Eng	gineer at	Flight	Research	Branch,	NASA
Langley. Mem	ber AIAA				
††Associate					
Aeronautical a	nd Materi	ials Eng	gineering.	Senior I	Member
AIAA.					

Copyright © 1992 by the American Institute of Aeronautics and Astronautics, Inc. No copyright is asserted in the United States under Title 17, U.S. Code. The U.S. Government has royalty-free license to exercise all rights under the copyright claimed herein for Governmental purposes. All other rights are reserved by the copyright owner.

# Nomenclature

b	wing span, ft
$c_{f_{\underline{a}}}$	skin-friction coefficient, τ/q
${\overset{C_f}{c_f}}^*$	Preston-tube-measured C <sub>f</sub> using eq. (1)
$C_L$	lift coefficient, lift/qS
$C_{\mathbf{n}}^{-}$	normal-force coefficient obtained from
	integrated pressures
$C_{\mathbf{p}}$	pressure coefficient, (p-p <sub>S</sub> )/q
	chord length, ft
$\frac{c}{c}$	mean aerodynamic chord, 11.20 ft
d	Preston-tube diameter, in
h	pressure altitude, ft
K	relaminarization parameter, eq. (3)
M	Mach number
p	local static pressure, psf
$p_S$	freestream static pressure, psf
p <sub>t</sub>	local total pressure, psf
q	freestream dynamic pressure, $\rho V^2/2$ , psf
$R_{\overline{c}}$	Reynolds number based on $\bar{c}$ , $V\bar{c}/v$
R	attachment-line Reynolds number, eq. (2)
S	reference wing area, 980 ft <sup>2</sup>
S	surface streamwise coordinate, ft
V	true airspeed, ft/sec
$V_{\mathbf{i}}$	indicated airspeed, knots
x/c	non-dimensional chordwise coordinate
У	spanwise coordinate, ft
z/c	non-dimensional thickness coordinate
α	aircraft angle of attack, deg
α <sub>2-D</sub>	local streamwise angle of attack, deg
Δp	differential Preston-tube pressure, p <sub>t</sub> - p, psf
$\delta_{ m f}$	flap deflection, deg
Λ	sweep angle, deg
η	non-dimensional spanwise location, y/(b/2)
ν	kinematic viscosity, ft <sup>2</sup> /sec
ρ	air density, slugs/ft <sup>3</sup>
θ	momentum thickness, ft
τ	shear stress, psf

# **Abbreviations**

ESP electronic scanning pressure KIAS knots indicated airspeed

2-D two-dimensional3-D three-dimensional

### Introduction

The design of high-lift system aerodynamics significantly impacts the overall design of transport aircraft in terms of sizing, performance, system complexity, and certification from safety and community-noise acceptance aspects. However, the design of subsonic high-lift systems remains a technical challenge mostly due to the complex flow physics associated with high-lift flows. High-lift flows are highly sensitive to Reynolds- and Mach-number effects. and therefore, difficult to predict from wind-tunnel or computational fluid dynamics (CFD) studies. In order to better understand high-lift flows and to correlate and validate results from wind tunnel and CFD, additional experimental data with sufficient flow details on 3-D swept wings are needed at flight Reynolds numbers. Thus far, flight investigations to obtain sufficiently detailed flow measurements on a high-lift system have been very limited. One such investigation was reported by Greff<sup>2</sup> on an Airbus A310-300 aircraft.

As part of a multi-phased research program at NASA Langley, flight tests are being conducted on the Transport Systems Research Vehicle (TSRV), a B737-100 aircraft, to obtain detailed full-scale flow measurements on a multi-element high-lift system at various flight conditions. In Phase I of the program, experiments were focussed on flow visualization, pressure distributions, and flow-separation measurements on the triple-slotted Fowler flap system of the research aircraft. Phase I activities have been completed, and the flight test results were reported by Vijgen, Hardin, and Yip.<sup>3</sup> In Phase II, more detailed flow measurements have been planned including the main wing and leading-edge slat components. Initial flight experiments for Phase II on the full-chord pressure distributions at one spanwise station were completed in February 1992. In Phase III, advanced instrumentation for detailed boundary-layer and wake flow-field characteristics are planned. Future flight experiments in both Phase II and III will provide detailed full-chord pressure measurements at several spanwise stations, and detailed boundary-layer measurements including attachment-line transition, relaminarization, laminar separation and reattachment, turbulent Reynolds stresses, confluent-flow development, and turbulent separation. The purpose of this paper is to present test results from initial Phase II flights as well as the status of the high-lift flight research program on the TSRV.

### Description of Flight Experiment

### Test Aircraft

The NASA Langley TSRV is the prototype aircraft used in the development of the Boeing B737-100 and has been significantly modified for flight systems

research.<sup>4</sup> The Boeing 737-100 is a twin-jet, shorthaul, subsonic transport designed to carry approximately 100 passengers with a cruise speed of Mach 0.78. In order to obtain short-field takeoff and landing performance, the aircraft incorporates a slat and triple-slotted flap high-lift system. Basic aerodynamic characteristics of the Boeing 737-100 configuration from wind-tunnel investigations have been documented in reports by Capone<sup>5</sup> and Paulson<sup>6</sup>.

Figure 1 shows the TSRV in flight during the conduct of the present high-lift experiments. Figure 2 shows a planform view of the B737-100 configuration and illustrates the overall geometric characteristics. The aircraft wing is characterized by a span of 93 ft, an aspect ratio of 8.82, and a sweep angle of 25° at the quarter-chord line and 27.58° at the leading edge outboard of the nacelle. Inboard leading-edge Krueger flaps and outboard leading-edge slats are extended in conjunction with the deflection of the triple-slotted trailing-edge flap system. As shown in figure 3, the outboard high-lift wing section studied in this paper consists of 5 elements: the leading-edge slat, the main wing with fixed leading edge, the fore flap, the mid flap, and the aft flap. At flap settings of 30° and 40°, the two most outboard slat segments are fully extended and deflected an additional increment from the 15° and 25° setting (see Fig. 3), effectively creating a spanwise break in the wing leading edge between the slats (see Fig. 4). For the 15°- and 25°-flap settings, only a very small slot exists between the slat and main-wing elements. The coves in figure 3 are shown streamlined for computational purposes; in actuality, the cove shapes are trailing-edge cutouts that are required for retracting the flap to the cruise setting.

# Instrumentation, Data Acquisition, and Data Reduction

Instrumentation for the full-chord, wing-section measurements is illustrated in figure 4. Surface static pressure distributions. Preston-tube skin-friction measurements, and flow visualization were made on an outboard wing section of the research aircraft. The chordwise pressure distributions were measured at a nominal spanwise station of  $\eta = 0.53$  on the upper and lower surfaces of the slat, main-wing, and flap elements using thin belts of plastic tubing (0.062 inch outside diameter) which were wrapped around each element. The belts were attached to the surface with thin (0.005 inch) adhesive tape. To minimize belt edge effects, five extra (non-functioning) tubes were added to each side, and the sides of each belt were smoothed with a siliconrubber compound. The technique of using external pressure belts has been commonly used in previous studies and was shown to provide good results when compared to flush surface orifices.<sup>7</sup> The possible effect of belts on the pressure distributions in the leading-edge regions of the present high-lift system will be determined in future flights with flush orifices. With the installation of the pressure belts, the minimum flap deflection was limited to 15°, while the standard maximum flap deflection of 40° was unchanged.

A total of 160 pressure tubes (144 for pressure distributions, 12 for static and total measurements of the Preston tubes, and 4 spare tubes) were connected to five electronically scanning pressure (ESP) modules which were located in the wing cove region. The ESP modules were maintained at a constant temperature to minimize zero shift of the measurement, and two differential-pressure transducer ranges (2.5 and 5 psi) allowed high resolution of the pressure data. A plenum chamber was housed in the wing cove region to provide the reference pressure for the ESP transducers; the reference pressure was monitored with an absolute pressure gauge and was related to the static pressure measured by the aircraft pitot-static probe. A small data-acquisition unit using single-board computer technology was located in the outboard flap track fairing of the wing (see Fig. 5) to access and address the ESP transducers. The digital output data were transmitted to a small, portable on-board computer for real-time display and stored on an optical disk for post-flight playback and data analysis. Pressures were recorded at a rate of 10 samples per second while aircraft flight parameters were recorded at a rate of 20 samples per second. The pneumatic lag for the longest tube length was measured in ground tests and determined to be approximately 0.5 seconds and was taken into account in the reduction of data.

In order to provide corrections of the static pressure due to probe position error for each flap setting, an airspeed calibration flight was conducted prior to the research flights using a tracking-radar method<sup>8</sup>. These corrections along with temperature measurements were used to compute freestream static and dynamic pressures as well as Mach and Reynolds numbers. Also, angleof-attack corrections were obtained by calibrating the aircraft angle-of-attack vane against pitch attitude obtained from the aircraft inertia navigation system in steady-state flight conditions. A control-surface potentiometer attached to the mid-flap provided deflection information of the trailing-flap system under loading during the flight. Lift coefficients were determined from steady-state, 1-g flight maneuvers using aircraft weight calculated from aircraft fuel consumption measured by fuel-flow sensors. Thrust corrections obtained from standard engine performance decks were applied to the lift data to account for the thrust contribution to lift.

Flow visualization was obtained by applying nylon yarn tufts to the upper surfaces of the outboard flap and the main-wing elements to indicate local regions of flow separation. The tuft patterns were recorded with still and video photography to allow for post-flight analysis and correlation. In addition, audio recording of pilots and flight test engineers on the video cassettes were used to discern quality of flight data samples.

In the present set of flight experiments, five Preston tubes were installed on the upper and lower surfaces of the main-wing element, and one Preston tube was installed on the slat upper surface (see Figs. 4 and 5). These probes contain a static orifice in addition to the pitot pressure orifice to measure total and static

pressures within the boundary layer. Preston-tube measurements near the trailing edge of the flap elements were obtained during the Phase I flights and were reported in reference 3. The local skin friction coefficient, C<sub>f</sub>, were determined based on the measured pressure differential at the tube using the Law-of-the-Wall calibration for turbulent flow. For the modified Preston tube used here, the wall shear stress was determined as follows: 9

$$\tau = \frac{\Delta p}{\left\{ A_1 \left[ \log_{10} \left( \frac{\Delta p \cdot d^2}{\rho v^2} \right) \right] - A_2 \right\}}$$
 (1)

where  $\Delta p$  represents the differential pressure measured by the Preston tube, d represents the outside diameter of the Preston tube, and A<sub>1</sub> and A<sub>2</sub> are calibration constants where  $A_1 = 38.85$ , and  $A_2 = 107.3$ . The outside diameters of the Preston tube were d = 0.083inches for the wing locations and d = 0.042 inches for the slat location. The above calibration expression is based on the assumption that the static and total ports of the probe are located within the region of the turbulent boundary layer that is governed by the Law-ofthe-Wall. Since the boundary-layer state as well as its thickness are dependent on the flap setting and the various flight parameters, it was uncertain that all Preston tubes would operate within the appropriate calibration range at all test conditions. Because of this uncertainty, Cf computations from the Preston-tube measurements using eq. (1) are listed in this paper as  $C_f^*$  to indicate that these measurements may not necessarily reflect actual skin-friction values if the Preston-tube readings were obtained outside the valid calibration range.

### Flight Test Conditions

The flight experiments covered a range of Reynolds and Mach numbers as the aircraft was flown to pressure altitudes of up to 20,000 feet. The chord Reynolds number, R<sub>c</sub>, ranged from 10 to 21 million, and the freestream Mach number varied from 0.16 to 0.40. Flap deflections of 15°, 25°, 30°, and 40° were investigated at pressure altitudes of 5,000 ft, 10,000 ft, 15,000 ft, and 20,000 ft. Test conditions and test points obtained in flight are shown in figure 6 as well as lines of constant Reynolds and Mach numbers for standard atmospheric conditions. As indicated by figure 6, flight at increasing altitudes provides conditions of increasing Mach numbers and decreasing Reynolds numbers for a given indicated airspeed, V<sub>i</sub>, which corresponds approximately to a constant lift coefficient for a given aircraft weight.

The flight-test points were obtained for each of the flap settings at approximately 1-g, steady-state conditions (that is, vertical acceleration near zero) in level flight with the aircraft initially flown at a high nominal airspeed and then slowed to the stick-shaker

speed. Data were sampled for approximately 30 seconds at each constant-airspeed test point. In addition, data were recorded during the deceleration of the aircraft between selected test points. The aircraft was decelerated at a nominal rate of 1 knot per 5 seconds while constant altitude was maintained. Pertinent test points were repeated to ensure data repeatability. All data were obtained with the landing gear retracted. The research flight deck<sup>4</sup> on the TSRV allowed auto-throttle and auto-pilot operations of the aircraft for airspeed- and altitude-hold modes of testing. Use of the auto-pilot operations increased the productivity of the flight test and enhanced the quality of the flight data sampled.

# Flight-Test Results and Discussion

### Trimmed-Lift Data

Trimmed-lift coefficients from representative flight data at h = 10,000 ft are shown in figure 7 for the TSRV configuration with flap defections of 15°, 25°, 30°, and 40°. For the angle-of-attack range tested, the lift curves remained nearly linear with no noticeable slope change except for a slight decrease in the lift-curve slope at high angles of attack for the 15°-flap case. Also, for the 30°- and 40°-flap settings, an increase in the lift-curve slope occurs at  $\alpha \approx 0^{\circ}$  and  $2^{\circ}$ , respectively. In figure 8, the flight lift data are compared with available wind-tunnel lift data<sup>6</sup> for the 30°- and 40°-flap settings. The wind-tunnel investigation used a 1/8-scale model of the TSRV with flow-through nacelles, and the data were obtained at test conditions of  $R_{\bar{c}} = 1.4$  million and M = 0.14. Wind-tunnel trimmed-lift coefficients were estimated by transferring the force and moment data to 18-percent c which corresponds to the nominal center-of-gravity location in flight. As expected, the comparison shows significant differences between flight and wind-tunnel data due to viscous (Reynolds-number) effects. Flight Reynolds numbers, ranging from about  $R_{\bar{c}} = 11$  million at the high-angle-of-attack (low-speed) conditions to about 18 million at low-angle-of-attack (high-speed) conditions, were significantly higher than the wind-tunnel Reynolds numbers. The comparison of figure 8 shows that flight lift data exhibit a steeper liftcurve slope than that of wind-tunnel lift data. Moreover, as discussed, the lift-curve slope in flight is nearly linear throughout the measured angle-of-attack range, whereas the lift curve slope from wind-tunnel data decreases with increasing angles of attack, indicating strong viscous effects. In the mid-angle-ofattack range, lift and incremental lift values between flap deflections of 30° and 40° were similar between flight and wind-tunnel data. However, at low angles of attack, the lift coefficients obtained in flight were overpredicted by the wind-tunnel data. overprediction may be a result of a reversed Reynoldsnumber effect on multi-element airfoils as discussed in investigations by Morgan et al. 10 and Woodward et al. 11 where lift decreases at higher Reynolds number. This lift loss, known as an inverse Reynolds-number effect, is caused by the relative thinning of the boundary layer in the slot gaps at higher Reynolds numbers. As

a result, the effective slot gaps are no longer at optimal conditions for generating lift. At higher angles of attack ( $\alpha \approx 10^{\circ}$  to 12°), the flight lift coefficients were severely underpredicted by the wind-tunnel data. This underprediction by the wind-tunnel data is likely due to premature flow separation experienced at the lower Reynolds number in the wind tunnel.

### Flow Measurements

In the analysis of flight data, it should be noted that test points were obtained at 1-g, level flight conditions where increasing angle of attack corresponds to slower airspeeds, and therefore, both the Reynolds number and the Mach number change with each test point (see Fig. 6). Overall pressure distributions measured on a highlift wing section of the TSRV are presented in figure 9 at various angles of attack for the 15°-, 25°-, 30°-, and 40°-flap cases from flight data at a test altitude of h = 10,000 ft. Results at other altitudes are similar in general. Several interesting points are noted for the overall pressure distributions: (1) The results indicate that increasing angle of attack primarily increased slat and main-wing pressure loading, but had little effect on the flap pressures for the angle-of-attack range tested. This result is explained by the dependence of the local flap-element angle of attack on the in-flow angle which is largely determined by the deflection angle of the preceding flap element. (2) The pressure data show that maximum C<sub>p</sub> values were less than the incompressible, 2-D value of 1.0 because of sweep effects. In threedimensional, swept-wing flows, an attachment line exists because of the spanwise velocity component, and therefore, the maximum  $C_D$  value is less than 1.0. Also, note the flow reattachment in the main-wing cove as indicated by C<sub>D</sub> values close to the leading-edge attachment-line values. (3) The trailing-edge pressures of each element, except for the aft flap, do not recover completely because of the influence of the downstream element on the flow field of the upstream element. Also, the accelerating flow region between the elements influences the trailing-edge pressure distributions. For example, note the increasing upward curvature of the main-wing element upper-surface pressures near the trailing edge with increasing flap deflection. This multi-element flow phenomenon is attributed to the "circulation effect" and "dumping effect" described by Smith<sup>12</sup>. The higher velocities near the trailing edge also relieve the pressure rise on the leading edge of the downstream element, thus alleviating potential separation problems that could cause loss in lift.

In order to show the relative contribution of each element to the total wing-section lift, pressures for each of the elements were integrated to provide section normal-force coefficients at selected angles of attack as shown in figure 10. The integrated pressures are weighted by the projected chord length of each element relative to the full wing chord. The results indicate that the wing and slat loadings increased with angle of attack while the flap loadings remained relatively constant. Also, a reduction in the normal-force curve is observed

for the main-wing element corresponding to the change in the aircraft lift-curve slope discussed (see Fig. 8).

A more detailed discussion of the pressure distributions of individual elements is presented in the following sections:

Flap-element flow characteristics. - A detailed study of the flap pressure distributions was presented in a paper by Vijgen et al.<sup>3</sup>, and therefore, discussion herein is limited only to the fore-flap element where flow separation occurred for 40°-flap deflection. The fore-flap pressure distributions from the present flight experiment were similar to those reported previously and are shown in detail in figure 11 for the 15°- and 40°-flap settings and several angles of attack. For the 15° case, increasing angle of attack increased the upper-surface loading slightly while the lower-surface pressures remained nearly unchanged. These increases in loading for the fore-flap element are small compared to the increases for the slat and main-wing elements. For the 40°-flap deflection, the upper surface loading did not increase as consistently with increasing angle of attack because of flow separation near the trailing edge of the fore flap. The upper surface pressures increased slightly from  $\alpha = -1.51^{\circ}$  to 2.47°, then remained nearly unchanged for  $\alpha = 7.70^{\circ}$  to 9.57°, and finally decreased at the highest angle of attack. Flow separation is indicated by the nearly constant pressure level near the trailing edge of the fore flap for most angles of attack. For the lowest angle of attack presented, the fore-flap pressures near the trailing edge do not indicate flow separation.

Flow visualization, shown in figure 12, using surface tufts from the present flight experiments also indicated fore-flap flow separation at the 40°-flap setting. For the 40°-flap setting, the tuft photo is shown with the aircraft flown at  $\alpha \approx 7^{\circ}$ . For this highlift condition, the flow patterns showed generally attached flow on the flap system, although, locally, in the wake of the flap track fairings, unsteady and separated flow regions were evident. In the region of the pressure belt location, the flow remained attached on the main wing and the flaps except for flow separation near the trailing edge of the fore-flap element. The tuft patterns indicate that flow separation occurred over approximately the last 20 percent of the fore-flap chord, which correlates well with the previously discussed observations based on the pressure distributions.

Previously published Preston-tube skin-friction measurements<sup>3</sup> are presented in figure 13 to further examine the fore-flap separation phenomena. Figure 13 shows the Preston-tube measurements obtained near the trailing edge of the fore-flap element as a function of angle of attack for the various flap deflections. Values of  $C_f^*$  near zero indicate flow separation at the Preston-tube location. The data of figure 13 indicate that the flow separated on the fore flap only at the 40°-flap setting; however, the  $C_f^*$  variation with  $\alpha$  is similar for the 30° and 40° settings. Also the  $C_f^*$  variation with  $\alpha$  for the 15° and 25° settings are similar, however, both show different trends compared to the

higher flap settings. The changes in Cf\* behavior between the 25° and 30° setting could be caused by the larger slat deflection for the higher flap settings (see Fig. 3), resulting in the presence of a thicker slat wake along the main-element upper surface and a change in the flow over the fore flap. The presence of a slat wake can result in a confluent boundary layer over the fore flap with two distinct wake portions, and a reduction in wall shear stress over the flap is expected as a consequence.

Main-element flow characteristics. - The main-wing pressure distributions are presented in more detail in figure 14 for the 15°- and 40°-flap settings and several angles of attack. In both cases, there is a large suction peak at the x/c = 0.12 location. This location corresponds to a pressure port that is located just behind the notch (i.e., a forward-facing step) in the leading-edge surface where the slat element would nest when retracted (see Fig. 5b). This notch caused a local flow acceleration that was registered by the pressure belt measurement. Also, the last 6 ports on the lower surface are actually locations on the lower surface of the spoiler and in a region of the wing cove where the flap elements would nest when retracted. Note that the lower-surface flow apparently re-attaches onto the spoiler lower surface as indicated by the high C<sub>D</sub> value which is similar to the attachment-line values near the leading edge. An influence of a lower-surface, slat separation bubble is evidenced by the reduction of the pressures in the lower-surface nose region. The influence of the separated-flow region along the lower surface of the slat can be noticed by the reduction in pressures in the lower-surface nose region  $(x/c_{main} \le$ 0.20). For the 15°-flap setting, the slat and main-wing elements form, in effect, a single element. The slot on the upper surface between the slat and the main-wing element is very small (see Fig. 3), causing the slat leading edge to function as the stagnation region for both the slat and the main-wing elements for low- and mid-range angles of attack. At the higher angles of attack in figure 14a, an attachment point exists also on the main-wing element for the 15°-flap setting. For the 40°-flap setting, the effect of the slat-cove separation region is noticeable only at very low angles of attack, reducing the maximum pressure on the lower nose region. Large flow accelerations as indicated by the drop in pressures near the leading-edge upper surface make this region conducive to relaminarization as studied in the paper by Vijgen et al.<sup>3</sup> For the 40°-flap case, the suction peak occurred at an x/c = 0.036 which is ahead of the notch in the surface and creates a doublepeaked pressure distribution for most of the angles of attack shown.

Preston-tube skin-friction measurements for the main-wing element are presented in figure 15 for the 15°- and 40°-flap cases as a function of angle of attack. Three upper-surface and two lower-surface Preston tubes were attached to the main-wing element (see Figs. 4 and 5). Probe no. 1U is located just behind the notch in the leading-edge upper surface (see Fig. 5b). For both the

15°- and 40°-flap cases, the data show that probe no. 1U experienced significantly high values of Cf\*. These high readings are indicative of the high flow velocities at that location. Also, in both cases, the lower-surface probe near the leading edge, probe no. 1L, experienced low values approaching zero at low angles of attack. This result is indicative of the lower-surface slat separation bubble at low angles of attack engulfing the main-wing leading-edge region on the lower surface. At 40°-flap setting, the slat is extended an additional deflection (see Figs. 3 and 5). For the 40°-flap case, the Cf\* values for the mid-chord location, probe no. 2U, and for the aft-chord location, probe no. 3U, exhibited higher values than those for the 15°-flap case. This result correlates with the opening of the slat gap, which allows higher velocity flows over this region and reduces the adverse pressure gradients for  $\delta_f = 40^\circ$ . Also, note the change in the probe readings at the aftchord location between  $\alpha = 3^{\circ}$  and  $7^{\circ}$ . This change in Cf\* correlates with changes in the boundary-layer state of the slat element discussed in the following sections.

Slat-element flow characteristics. - The slat pressure distributions are presented in more detail in figure 16 for the 15°- and 40°-flap settings and several angles of attack. On the lower surface, slat pressure ports aft of x/c = 0.30 were actually located in the slat cove (see Fig. 3). The approximate position of the attachment line is indicated by the maximum C<sub>D</sub> value. For both flap settings, the attachment line is located on the upper surface of the slat for angles of attack less than about 4°. Consequently, for the 40°-flap setting and  $\alpha = -1.51^{\circ}$ , the slat is shown to produce negative lift (see Fig. 10b). At this condition the existence of a laminar separation bubble on the lower surface is evidenced by the nearly constant C<sub>p</sub> value in the range of 0.05 < x/c < 0.15. Another interesting point is the nearly constant pressure level in the slat cove region aft of x/c = 0.30 for both flap settings at high angles of attack. This is indicative of the separated flow region in the cove. Near the lower-surface trailing edge, the pressure distributions indicate increasing flow velocities as a result of the slot flow between the slat and the main-wing elements. For a given angle of attack, a comparison of the pressure distributions for the 15°- and 40°-flap setting shows that they are very similar (e.g., note the pressure distributions at  $\alpha \approx 2.5^{\circ}$ , 9.5°, and 13.5°). At low angles of attack, the upper-surface pressures exhibited favorable gradients from the leading edge on. At  $\alpha \approx 8^{\circ}$ , the upper-surface exhibited a nearly flat pressure distribution for most of the slat chord. At higher angles of attack, a pressure peak developed near the upper-surface leading edge with a subsequent adverse gradient downstream. For the 15°-flap setting, a minimum value of  $C_p$  = -13.18 is reached at the near-stall condition of  $\alpha$  = 16.42°. This  $C_p$  value corresponds to a local Mach number of 0.83 even though the freestream Mach number was only 0.20. Although sonic conditions were not experienced in the present flight experiment, these high Mach-number

values can significantly influence the flow behavior and performance of high-lift systems.

In figure 17, the Preston-tube measurements on the slat are plotted as a function of aircraft angle of attack for two altitudes, h = 10,000 ft and 20,000 ft, and two flap settings,  $\delta_f = 15^{\circ}$  and 40°. For both flap settings, the data show a significant increase in Cf\* in the midangle-of-attack range. These measurements are examined first for the 40°-flap setting in figure 17b. At low angles of attack ( $\alpha < 2.5^{\circ}$ ) and at high angles of attack ( $\alpha > 9.0^{\circ}$ ), the measurements show trends that are similar to those of the main-wing element probe 1U. However, at intermediate angles of attack, the results indicate a dramatic increase in the measured values for Cf\*. This increase can be traced to a sudden increase in the total-pressure reading of the Preston tube, whereas its static-pressure reading was shown to vary smoothly throughout this angle-of-attack range. This behavior can be related to the attachment-line boundary-layer state and the phenomenon of relaminarization as discussed in the following section.

### Attachment-Line Transition and Relaminarization

In three-dimensional flows, transition can occur at higher Reynolds numbers at the attachment line near the leading edge, thereby significantly influencing the downstream turbulent flow field, i.e. - confluent boundary layers and onset of separation. Depending on the pressure distribution, the leading-edge sweep angle, and the Reynolds number, the attachment line can be laminar, transitional, or turbulent. 13, 14, 15 Relaminarization of the flow downstream of a turbulent attachment line can occur if the streamwise flow acceleration is sufficiently strong. 16,17,18 If the flow ahead of the steep adverse pressure gradient along the upper surface of the elements is laminar, significant Reynolds-number effects can occur due to the presence of a laminar-separation bubble in this region. In a high-Reynolds-number wind-tunnel investigation on swept wings, maximum-lift losses of the order of 15 percent have been measured when transition occurred along the attachment line. 19 The issue of relaminarization is of importance in the extrapolation of sub-scale three-dimensional wind-tunnel results to flight Reynolds numbers. Attachment-line transition and the possibility for relaminarization along the five elements of the B737-100 geometry were examined by Vijgen et al.<sup>3</sup> using the predicted pressure distribution. Results of the study indicate that the attachment line along the slat and fore flap are likely to be laminar, while the attachment line along the fixed leading edge (main element) is likely to be turbulent for the 40°-flap setting at  $\alpha = 0^{\circ}$ . The attachment line along the slat was measured to be laminar under certain high-lift flight conditions in a previous flight experiment as reported by Greff<sup>2</sup> on an Airbus A310-300 aircraft. As calculated by Vijgen et al.3, laminar attachment-line conditions are expected on the B737-100 configuration.

An important parameter when examining the characteristics of the attachment-line boundary layer

along the leading edge of a swept  $\underline{\text{lifting}}$  surface is the attachment-line Reynolds number,  $\overline{R}$ , as defined by the following equation:

$$\overline{R} = \frac{W_{\infty} \kappa}{v}$$
where 
$$W_{\infty} = V \sin \Lambda$$
and 
$$\kappa = (v/U')^{0.5}$$

The characteristic velocity, W<sub>∞</sub>, is the spanwise component of the freestream velocity, and  $\kappa$  is the characteristic length where U' represents the inviscid velocity gradient at the attachment line in the direction normal to the attachment line. 13,14,15 For a laminar attachment-line boundary layer along an infinite swept cylinder, the momentum thickness can be shown to be  $\theta = 0.404 \text{ K}$ , and consequently,  $R_{\theta} = 0.404 \text{ R}.^{20}$ Previous studies have shown that for R < 245, the attachment-line boundary layer will tend to remain laminar, and turbulent contamination introduced in the boundary layer by surface roughness and intersecting turbulent shear layers will decay. For R > 245, the turbulence will self-sustain, causing the attachment-line flow as well as the flow downstream of the attachment line to become turbulent. In the absence of roughness and intersecting turbulent shear layers, attachment-line instability will occur only if  $\overline{R} > 580.21$ 

Using the measured pressure distributions (Fig. 16), R is calculated and plotted in figure 18. The results show that the slat attachment line is expected to be laminar for most test conditions at a 40°-flap setting. However, it should be noted that the Preston tube was located just outboard of the pressure belts (see Fig. 5), and these belts will cause the attachment line to become turbulent immediately downstream of the belts. For R < 245, the turbulence introduced into the attachmentline boundary layer by the belts will decay. A comparison with Gaster's experimental results 14 depicting the decay of turbulence behind trip wires on the attachment line indicates that the Preston tube on the slat was located in the turbulent-flow region. This introduction of turbulence explains the turbulent reading by the probe at low and high angles of attack in spite of low values of R, but this does not explain the increase in Cf\* at intermediate angles of attack. To explain this result, the possibility of relaminarization is analyzed for the slat region.

An important parameter when examining relaminarization is the inverse Reynolds number parameter, K, which is defined as follows:

$$K = \left(\frac{U\zeta}{V}\right)^{-1} \tag{3}$$

where the characteristic velocity is represented by the local inviscid velocity, U, and the characteristic length,  $\zeta$ , is defined by  $\zeta = U/U_s$  with  $U_s$  representing the

velocity gradient along the inviscid streamline.  $^{16,22,23}$  Reversion of the boundary layer from the turbulent to the laminar state is shown to occur for K values greater than approximately 3 x  $^{10^{-6}}$  for 2-D flows (only very limited detailed data are available for 3-D flows on swept wings $^{17,18}$ ). In figure 18b, the maximum value for K, as calculated from the measured pressure distributions (assuming locally infinite swept wing conditions), is plotted in addition to R. The results indicate that relaminarization, based on K = 3 x  $^{10^{-6}}$ , is expected to occur for angles of attack greater than approximately  $^{2.5^{\circ}}$ ; a value that is in markedly good agreement with the lowest angle of attack at which the sudden increase in  $^{16.22,23}$ 

Relaminarization produces a significant reduction in boundary-layer thickness, and this caused the Preston probe to be only partially submersed in the boundary layer as compared to being fully submersed in the turbulent case. The end result was an increase in the total-pressure reading of the Preston tube, and therefore, an accompanying increase in the value of  $C_f^*$  resulted. Thus, the increase in  $C_f^*$  in the intermediate angle-of-attack range appears to indicate a laminar boundary-layer state at the Preston tube.

The drop in  $C_f^*$  at  $\alpha \approx 9^\circ$  to a turbulent value indicates that the boundary-layer state has become turbulent again. This change in boundary-layer state is explained by the development of a suction peak on the slat upper surface near its leading edge at this angle of attack (see Fig. 16). The suction pressure peak causes laminar separation, transition from laminar to turbulent flow in the free shear layer, and reattachment of the boundary layer in the turbulent state ahead of the Preston tube.

Based on these results for the 40°-flap case, the use of the relaminarization parameter, K, appears to be sufficiently accurate to predict the occurrence of relaminarization in highly accelerated flows. However, the results in figures 17 and 18 for the 15°-flap setting show that a parameter based on a local Reynolds number is not adequate to capture all the flow physics of the relaminarization process for 3-D flows. For the 15°-flap setting, the increase in Cf\* first occurred at approximately  $\alpha \approx 7^{\circ}$  and h = 20,000 ft and did not occur at all at h = 10,000 ft. The results of figure 18 show that in this case K<sub>max</sub> values must be larger than approximately 6 x 10<sup>-6</sup> for relaminarization to occur. Also, in this case, the demise of laminar flow at the Preston tube can be correlated with laminar separation and transition ahead of the probe. Future flight experiment using hot films, boundary-layer rakes, and flush-mounted pressure ports will allow the study of the relaminarization process in more detail.

## Computational Analysis of Pressure Measurements

A limited analysis of the experimental pressure distributions is presented using a 2-D, viscous, multielement panel code. The current lack of threedimensional confluent boundary-layer multi-element analysis methods, necessitates the use of two-

dimensional methods in conjunction with simple-sweep theory for the analysis of 3-D high-lift systems.<sup>24</sup> The 2-D, viscous, multi-element code used for the analysis of the in-flight pressure measurements in this paper is the Multi-Component Airfoil (MCARF) computer code<sup>25,26</sup>, a widely-used aerodynamic analysis method for two-dimensional, multi-element airfoils. MCARF employs potential-flow and confluent, integral boundary-layer methods to predict the viscous-flow properties over multi-element airfoils. The sectional geometries used in the computational analyses are shown in figure 3. The actual cove shapes of the slat, main-wing, fore-flap, and mid-flap elements have been replaced by smoothly faired shapes to facilitate the flow calculations. In the present analysis, simple-sweep theory, described in the paper by Lock<sup>27</sup>, is used to account for sweep effects. One of the challenges in the application of 2-D calculations to 3-D results is the determination of the local angle of attack, Q2-D, for the two-dimensional methods. One method to determine local angles of attack is to use the spanload lift distribution calculated by simple vortex-lattice methods for the TSRV wing with flaps deflected and account for the trimmed-lift decrement due to the horizontal tail. Preliminary evaluation of this procedure using recent measurements of the full-chord wing-section pressures on the TSRV aircraft showed reasonable results using this method.<sup>28</sup> Because experimental slat pressures are now available, another method is used to more accurately determine the 2-D angle of attack for computational purposes. Typically, the full-chord pressure distributions are integrated, and the resulting section normal-force coefficient is matched with the computational section-normal-force coefficient. For a multi-element airfoil, where confluent boundary layer effects can become significant, a better approach should be the matching of experimental and computational pressure distributions on the slat upper surface. By using the slat pressures only, the effects of confluent boundary layers may be ignored in the determination of

Using this procedure to determine \$\alpha\_{2-D}\$, predicted pressure distributions are compared to flight-measured pressure distributions in figure 19. The comparison shows that the predicted pressure distributions are in reasonable agreement with flight-measured pressures for flap settings of 15° and 40° at the angles of attack shown. For the 15° case, where flow separation on the flap was not measured, the agreement is good. However, separated flows on the lower slat-cove and the main-wing lower-surface leading edge are not well predicted, and the suction peak on the main-wing element is not predicted because the notch is smoothed in the MCARF computations. For the 40°-flap setting, where flow separation was measured on the fore flap, the pressures over the fore flap are substantially overpredicted. Although the flow separation near the trailing edge is not modeled in MCARF calculations, the location of separation onset is predicted and is in agreement with the experimental separation location on the fore flap.<sup>3</sup> In addition, pressures are overpredicted

for the leading-edge upper surfaces for all the elements aft of the slat. This overprediction of the pressures suggests that modeling of the confluent boundary layers as well as three-dimensional sweep effects is not adequate for the complex high-lift geometry studied.

# Program Status and Future Plans

Future flight experiments on the TSRV high-lift configuration are planned to provide detailed measurements that address several of the critical multielement flow issues. Of particular interest are investigations of flows over the leading-edges including the transition locations, the slat- and main-wing-cove flows, confluent boundary layers including the interaction of the slat wake with the flow over the main-wing and the fore-flap elements, and off-body wake flows. The in-flight flow measurements should provide currently unavailable flow details at full-scale flight Reynolds numbers for correlation of ground-based wind-tunnel results and a challenging validation test case for CFD analysis, particularly in the modeling of 3-D confluent boundary-layer and separation phenomena.

Figure 20 illustrates the instrumentation for Phase-II flight experiments planned in 1993. Slat, wing spoiler, and flap spare parts have been obtained for use in these flights, allowing instrumentation to be embedded in the surfaces. A number of multi-channel ESP transducers will be used to obtain almost instantaneous pressure reading over a total of about 1200 pressure ports. Detailed pressure distributions will be obtained at several spanwise wing stations. Flush ports will be installed for the slat, wing spoiler, and flap elements. Pressure belts are still needed for the main-wing element because of the "wet wing" for storing fuel. Hot-film sensors will be installed along the slat, main-wing, and fore-flap leading-edge surfaces to detect transition, attachment-line, and separation characteristics. Boundary-layer rakes will be installed to determine the effect of slat wake on the main-wing flow. Because of the large number of sensors, a comprehensive data-acquisition system for flight is being developed to handle the large volume of pressure and hot-film anemometer data. A multi-channel anemometer data acquisition system with digital storage capability is planned in order to expedite the analysis of the high-frequency measurements. In addition to instrumentation for flow measurements, flow visualization including an emitting fluid technique<sup>29</sup> are planned to provide further understanding of the flow physics on a high-lift system. Also, structuraldeformation measurements are required to correlate the flight data with ground-based wind-tunnel and CFD results. These Phase-II flight experiments are planned to be conducted during calendar year 1993.

## Summary of Results

Flight experiments are being conducted as part of a multi-phased subsonic transport high-lift research program for correlation with ground-based wind-tunnel and computational results. The NASA Langley TSRV

(B737-100 aircraft) is used to obtain flow characteristics at full-scale Reynolds numbers to contribute to the understanding of several dominant high-lift flow issues such as boundary-layer transition, confluent boundary-layer development, and three-dimensional flow separation. This paper presents recent test results from initial Phase II efforts obtained for a full-chord wing section including the slat, main-wing, and flap elements.

The present flight experiment includes pressure distributions, Preston-tube skin-friction measurements, and surface-flow visualization over a full-chord wing section on a triple-slotted flap high-lift system for the 15°-, 25°-, 30°-, and 40°- flap settings. In a comparison with wind-tunnel trimmed-lift coefficients, flight data differed, as expected, due to viscous (Reynolds-number) effects. The flight-test data exhibited more linear lift curves and steeper lift-curve slopes for all flap settings. Measurements of the pressure distributions showed that increasing angle of attack primarily increased slat and main-wing pressure loading, but had only a small effect on the flap-element loading. For the 40°-flap deflection, the upper surface pressures indicated flow separation near the trailing edge at all but the lowest angles of attack. Tuft-flow visualization results corroborated the separation on the fore-flap trailing edge. Pressure distributions for the slat and main-wing elements showed lower-surface separation and re-attachment variations and aft movements of the attachment-line location with angle of attack. Pressure distributions on the slat upper surface reached high suction values which corresponded to locally high, subsonic Mach numbers.

Preston-tube measurements on the slat showed a dramatic increase in the measured values for  $C_f^*$  for certain conditions of angle of attack and altitude, indicating a laminar boundary-layer state at the Preston tube. These high readings of the Preston-tube probes were explained by relaminarization of the flow caused by the large favorable pressure gradients about the leading edge.

A limited analysis of the experimental pressure distributions using a 2-D, viscous, multi-element panel code showed that predicted pressure distributions were in reasonable agreement with flight-measured pressures for a range of angles of attack for flap settings of 15° and 40°. For the 15°-flap case, where flow separation was not measured, the agreement is good. For the 40°-flap setting, where flow separation was measured, the pressures over the flap elements were overpredicted. This overprediction of the pressures suggests that modeling of the confluent boundary-layer and three-dimensional sweep effects is not adequate for the present, complex high-lift geometry studied.

Future flight experiments on the TSRV high-lift configuration are planned to provide detailed measurements that address several of the critical multi-element flow issues. Of particular interest are investigations of flow over the leading-edge, transition locations, slat- and main-wing-cove flows, confluent boundary layers including the interaction of the slat wake with the main-wing and the fore-flap elements,

and off-body wake flows. Planned in-flight flow measurements will provide currently unavailable flow details at full-scale flight Reynolds number for correlation of ground-based wind-tunnel results and present a challenging case for CFD, particularly in the modeling of 3-D confluent boundary-layer and separation phenomena.

### Acknowledgements

The work of the second author was supported under NASA Langley Contract NAS1-18240 and NAS1-19299. The work of the third author was supported under NASA Langley Contract NAS1-19000. The work of the fourth author was supported in part under NASA Langley Cooperative Agreement NCC1-163.

# References

- <sup>1</sup> Dillner, B., May, F.W., and McMasters, J.H., Aerodynamic Issues in the Design of High-Lift Systems for Transport Aircraft," AGARD-CP-365, May 1984.
- <sup>2</sup>Greff, E., "In-Flight Measurement of Static Pressures and Boundary Layer State with Integrated Sensors," *Journal* of Aircraft, Vol.28, May 1991, pp. 289-299.
- <sup>3</sup> Vijgen, P.M.H.W., Hardin, J.D., and Yip, L.P., "Flow Prediction over a Transport Multi-Element High-Lift System and Comparison with Flight Measurements," presented at the Fifth Symposium on Numerical and Physical Aspects of Aerodynamic Flows, January 1992.
- <sup>4</sup>White, J.J., "Advanced Transport Operating Systems Program," SAE Paper 901969, October 1990.
- <sup>5</sup>Capone, F J., "Longitudinal Aerodynamic Characteristics of a Twin-Turbofan Subsonic Transport with Nacelles Mounted Under the Wings," NASA TN D-5971, October 1970.
- <sup>6</sup>Paulson, J.W., "Wind-Tunnel Results of the Aerodynamic Characteristics of a 1/8-Scale Model of a Twin-Engine Short-Haul Transport," NASA TM X-74011, April 1977.
- Montoya, L.C., and Lux, D.P., "Comparison of Wing Pressure Distribution from Flight Tests of Flush and External Orifices for Mach Numbers from 0.50 to 0.97," NASA TM X-56032, April 1975.
- <sup>8</sup>Gracey, W., "Measurement of Aircraft Speed and Altitude," NASA RP 1046, May 1980.
- <sup>9</sup>Bertelrud, A. "Total Head/Static Measurement of Skin Friction and Surface Pressure," AIAA Journal, Vol. 15, No. 3, March 1977, pp. 436-438.
- <sup>10</sup>Morgan, H.L., Ferris, J.C., and McGhee, R.J., "A Study of High-Lift Airfoils at High Reynolds Numbers in the Langley Low-Turbulence Pressure Tunnel," NASA TM 89125, July 1987.
- <sup>11</sup>Woodward, D.S., Hardy, B.C., and Ashill, P.R., "Some Types of Scale Effect in Low-Speed High-Lift Flows," ICAS Paper 4.9.3, 1988.
- 12Smith, A.M.O., "High-Lift Aerodynamics," Journal of Aircraft, Vol. 12, No. 6, June 1975, pp. 501-530.
- <sup>13</sup>Pfenninger, W., "Laminar Flow Control Laminarization, USAF and NAVY Sponsored Northrop LFC Research Between 1949 and 1967," in *Special Course on Concepts* for Drag Reduction, AGARD Report No. 654, March 1977, pp. 3-1 to 3-75.

- 14Gaster, M., "On the Flow Along Swept Leading Edges," The Aeronautical Quarterly, Vol. 18, May 1967, pp. 165 - 184.
- 15 Poll, D. I. A., "Transition in the Infinite-Swept Attachment-Line Boundary-Layer," The Aeronautical Quarterly, Vol. 30, part 4, November 1979, pp. 607-629.
- 16 Launder, B. E., and Jones, W. P., "On the Prediction of Relaminarization," ARC CP 1036, 1969.
- 17Hardy, B. C., "Experimental Investigation of Attachment-Line Transition in Low-Speed High-Lift Wind-Tunnel Testing," AGARD CP 438, Proceedings of the Symposium on Fluid Dynamics of Three-Dimensional Turbulent Shear Flows and Transition, Turkey, 1988, pp. 2-1 to 2-17.
- 18 Arnal, D., and Juillen, J. C., "Leading-Edge Contamination and Relaminarization on a Swept Wing at Incidence," Fourth Symposium on Numerical and Physical aspects of Aerodynamic Flows, edited by T. Cebeci, Cal. State University, Long Beach, CA, January 1989. 11 p.
- 19 Garner, P.L., Meredith, P.T., and Stoner, R.C., "Areas for Future CFD Development as Illustrated by Transport Aircraft Applications," AIAA Paper 91-1527-CP, June 1991.
- 20Crabtree, L.F., Küchemann, D., and Sowerby, L., "Three-Dimensional Boundary Layers," in *Laminar Boundary Layers*, Rosenhead, L. (ed.), Oxford Press, 1963.
- 21 Hall, P., Malik, M. R., and Poll, D.I.A., "On the Stability of an Infinite Swept Attachment Line Boundary Layer," *Proc. R. Soc. Lond.*, A395, pp. 229-245, 1984.
- <sup>22</sup> Narasimha, R. and Sreenivasam, K.R., "Relaminarization of Fluid Flows," Advances in Applied Mechanics, Vol. 19, 1979, pp. 221-309.
- 23Beasley, J.A., "Calculation of the Laminar Boundary Layer and Prediction of Transition on a Sheared Wing," ARC R&M 3787, 1976.
- 24Brune, G. W., and McMasters, J. H., "Computational Aerodynamics Applied to High-Lift Systems," Progress in Aeronautics and Astronautics: Applied Computational Aerodynamics, Vol. 125, AIAA, New York, 1990, pp. 389 - 433.
- 25 Stevens, W.A., Goradia, S. H., and Braden, J. A., "Mathematical Model for Two-Dimensional Multi-Component Airfoils in Viscous Flows," NASA CR-1843, 1971.
- 26Brune, G.W., Manke, J.W., "An Improved Version of the NASA-Lockheed Multielement Airfoil Analysis Computer Program," NASA CR-145323, 1978.
- 27Lock, R.C., "Equivalence Law Relating Three- and Two-Dimensional Pressure Distribution," ARC R&M 3346, May 1962.
- 28Hardin, J.D., "Computational Aerodynamic Analysis of a Transport High-Lift System and Comparison with Flight Measurements," Master's thesis, North Carolina State University, May 1992.
- 29 Fisher, D.F., and Meyer, R.R., "Flow Visualization Techniques for Flight Research," NASA TM-100455, 1988.



Figure 1. NASA Langley TSRV (B737-100 aircraft) during high-lift flight tests.

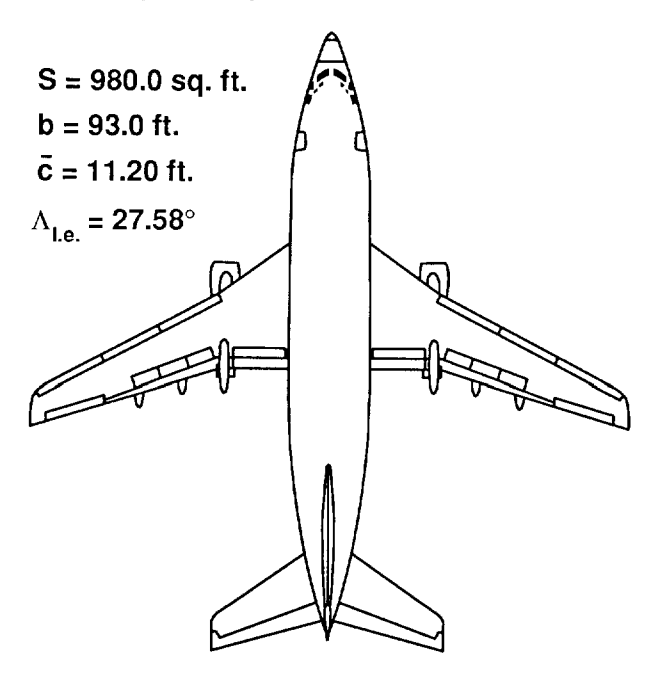


Figure 2. Planform view of the TSRV.

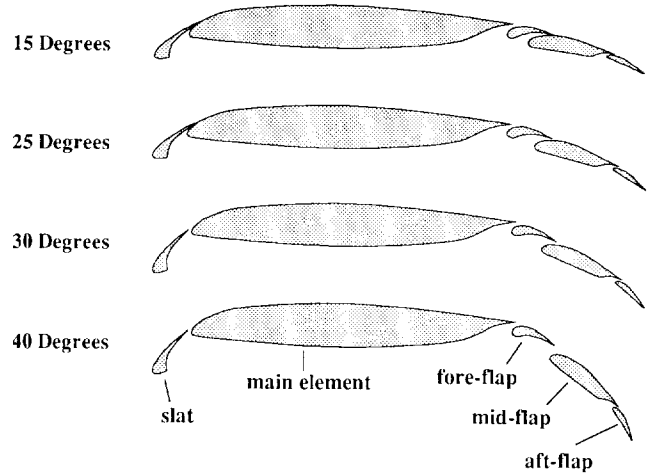


Figure 3. Multi-element section geometry of the TSRV for four flap settings.

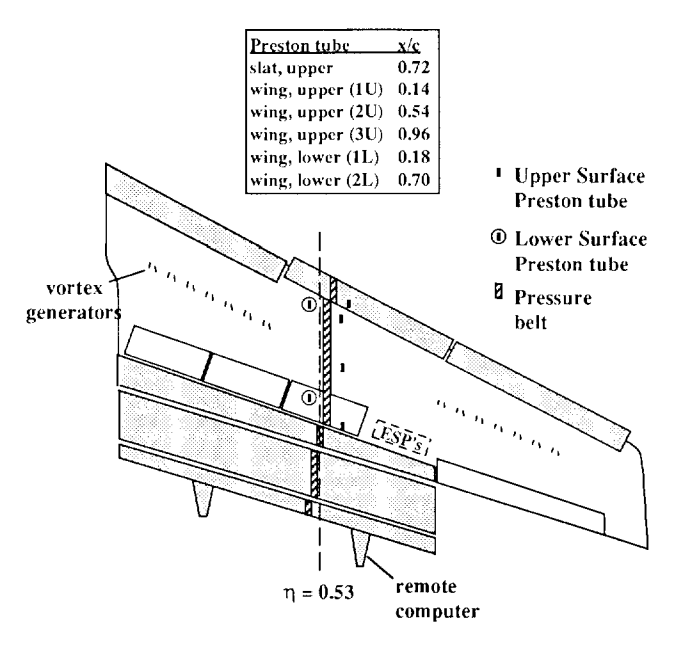


Figure 4. TSRV high-lift instrumentation layout. Wing shown at  $40^{\circ}$  flap setting.

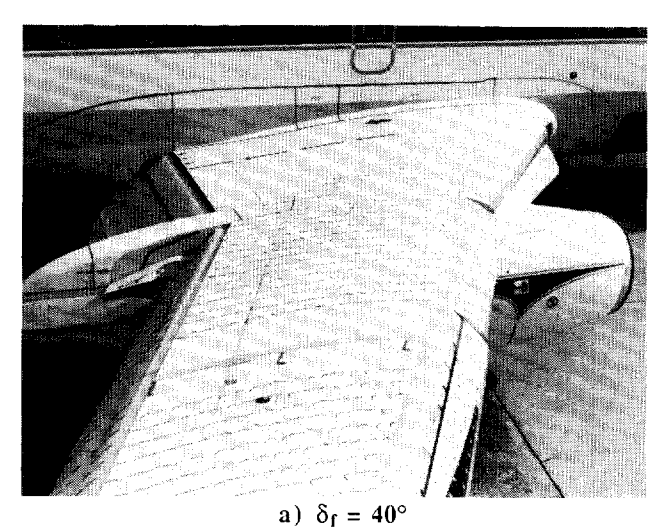
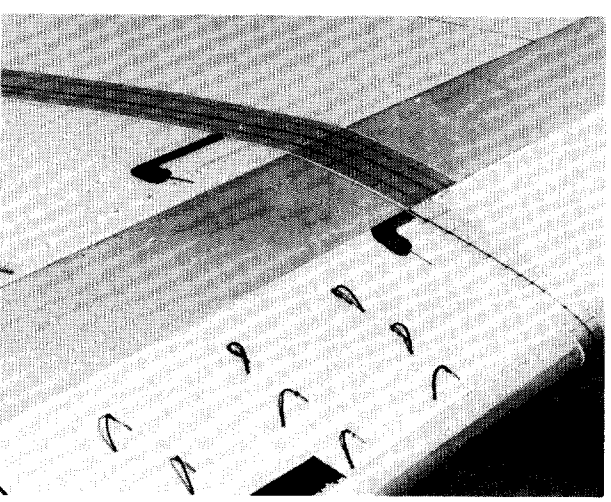


Figure 5. Pressure belt and Preston tube installation.



 $b) \ Close-up \ view. \ \delta_f = 15^{\circ}$  Figure 5. Concluded.

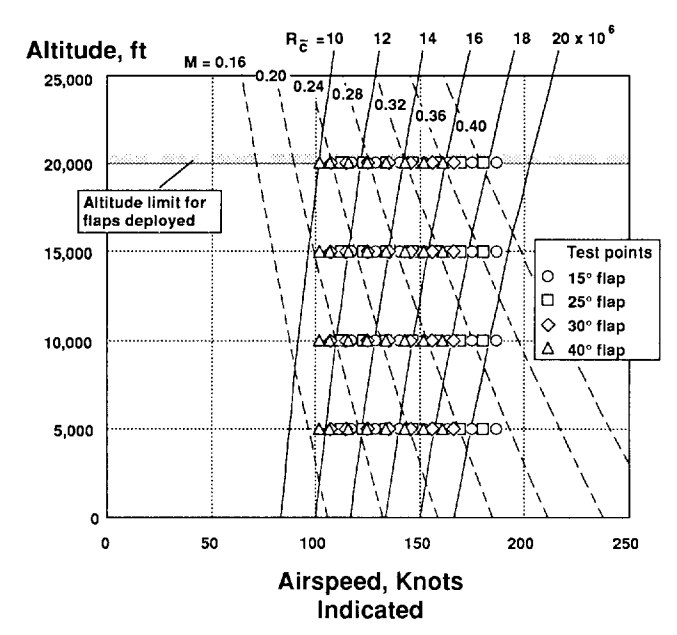


Figure 6. Flight-test conditions and test points.

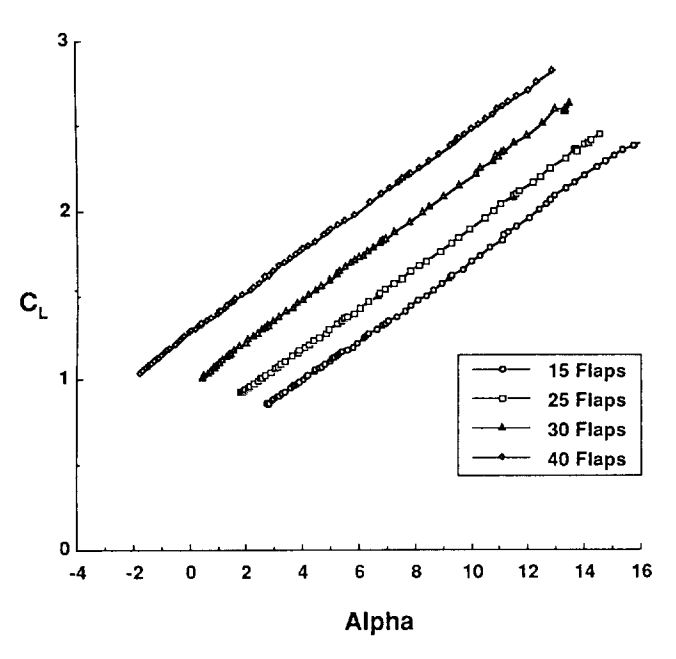


Figure 7. Trimmed-lift measurements for four flap settings.  $h=10,\!000\,$  ft.

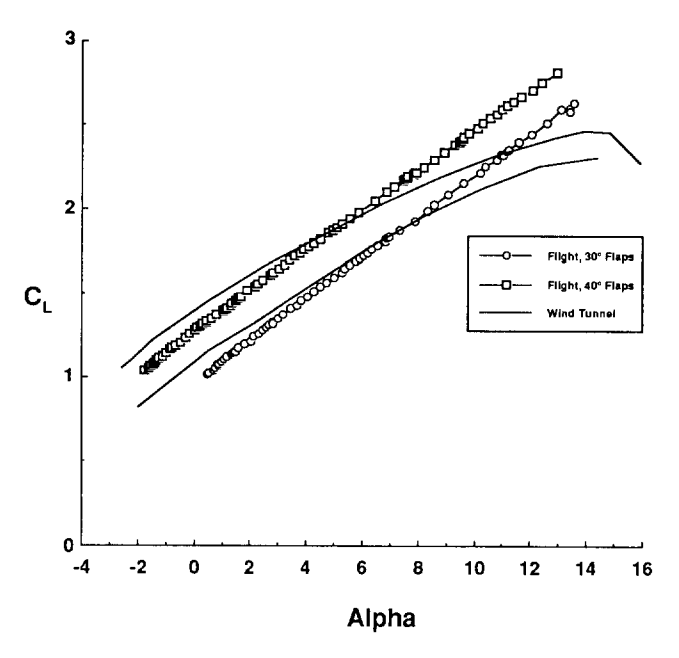
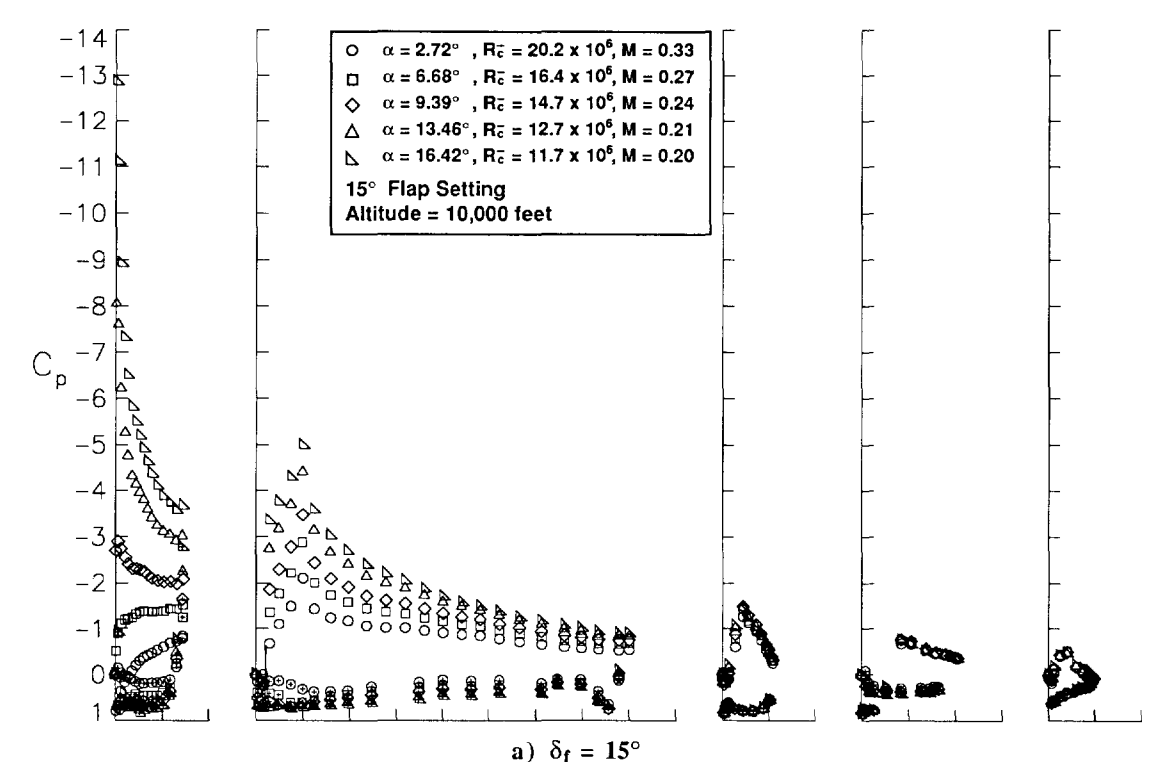


Figure 8. Comparison of flight and wind-tunnel trimmed-lift measurements. Flight-test data at  $h=10,000\,$  ft.



a)  $\delta_f=15^\circ$  Figure 9. Effect of angle of attack on measured pressure distributions. h = 10,000 ft

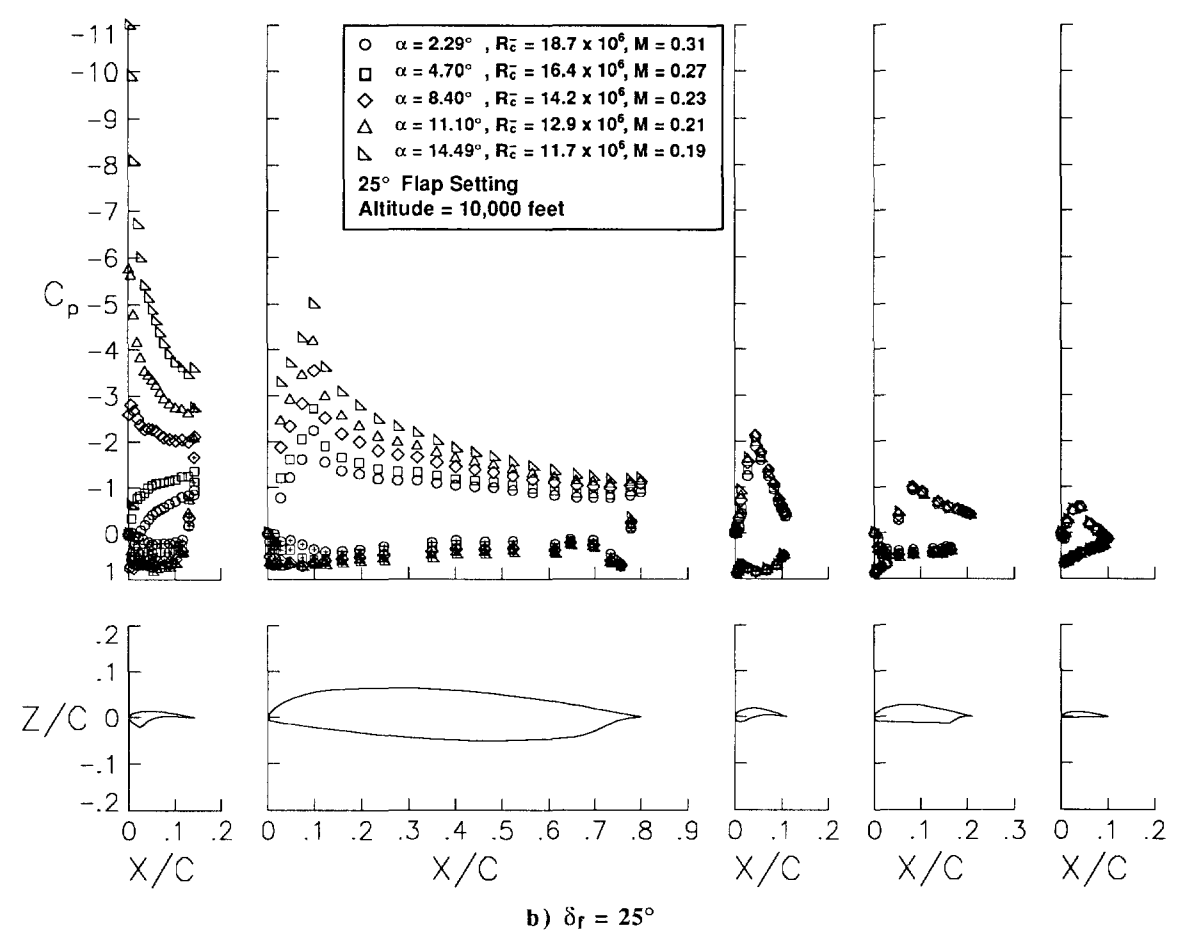


Figure 9. Continued.

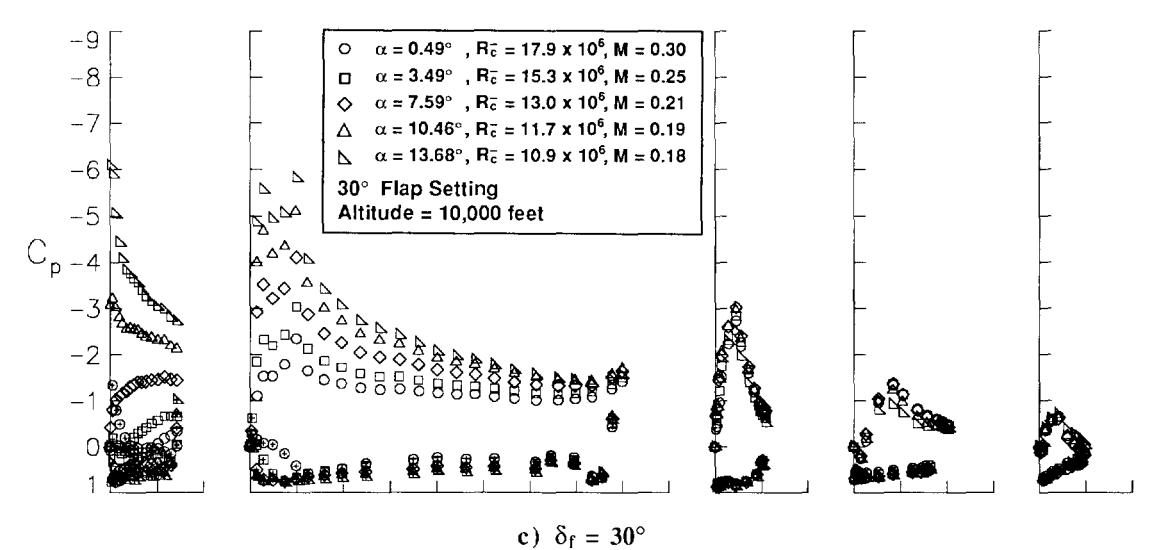


Figure 9. Continued.

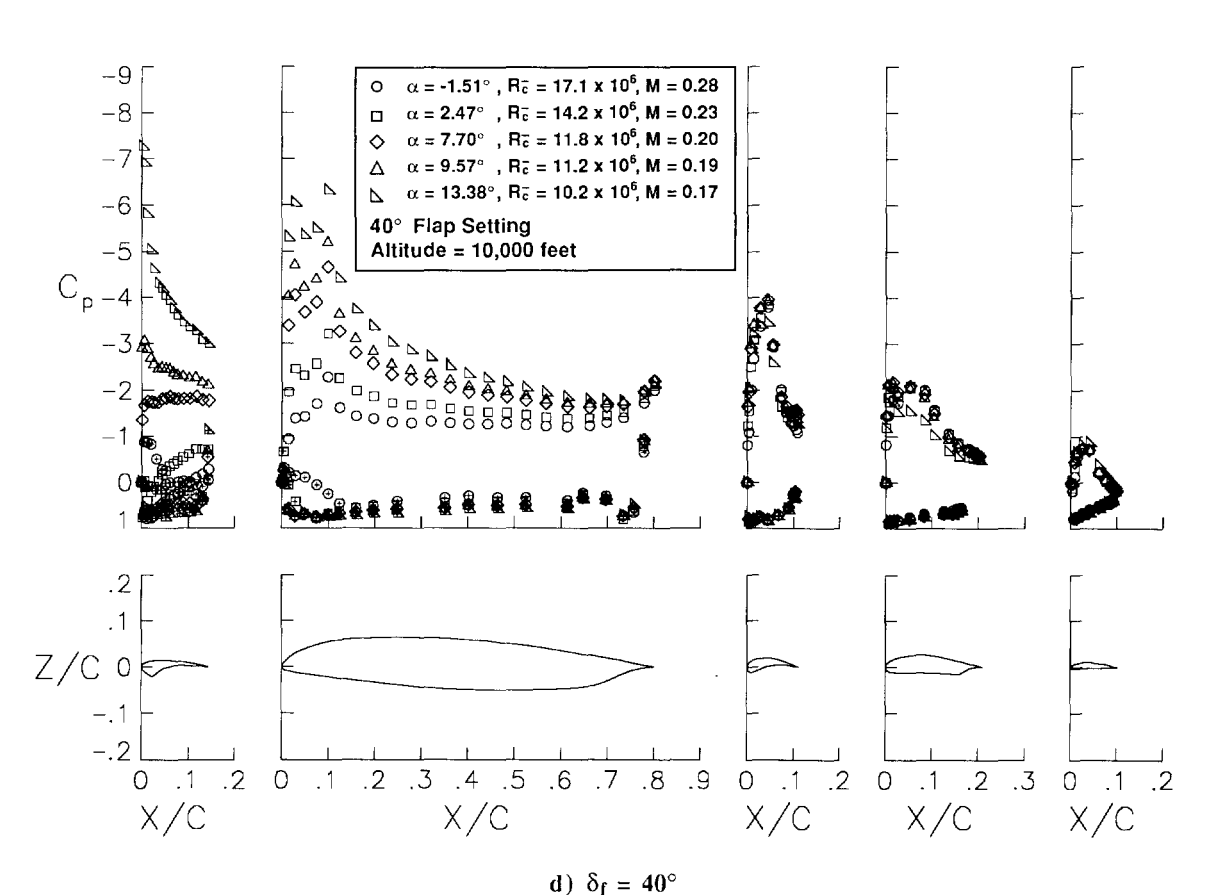


Figure 9. Concluded.

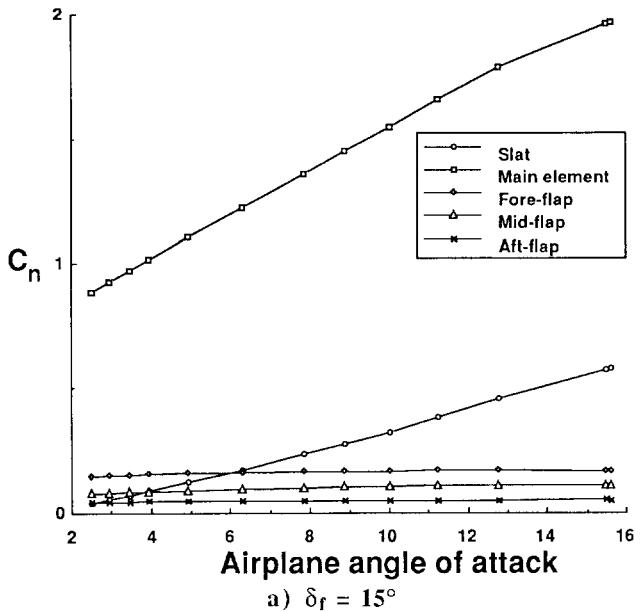


Figure 10. Element normal force coefficients from integrated pressure distributions. h = 10,000 ft.

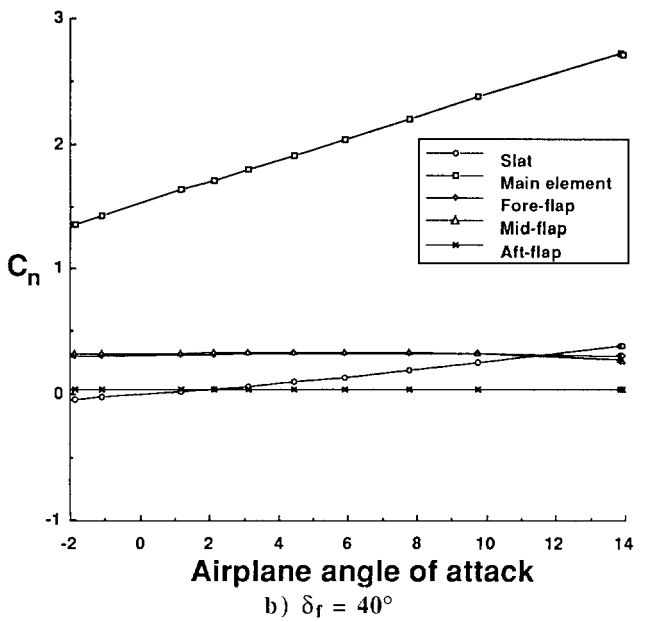


Figure 10. Concluded.

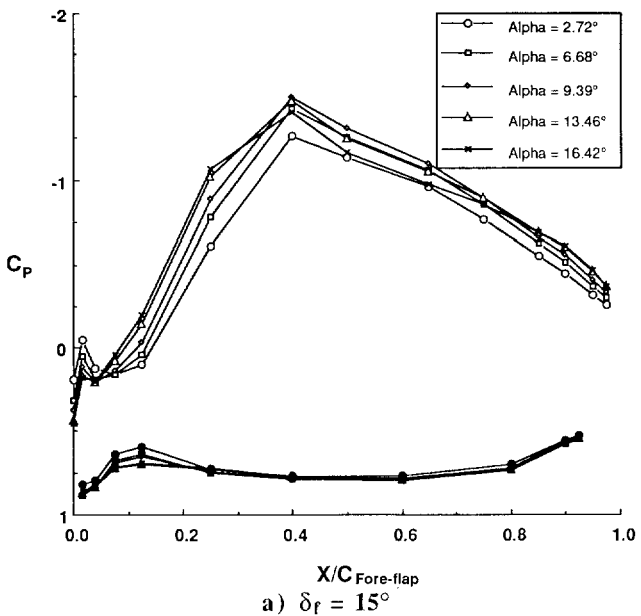


Figure 11. Measured fore-flap pressure distributions.

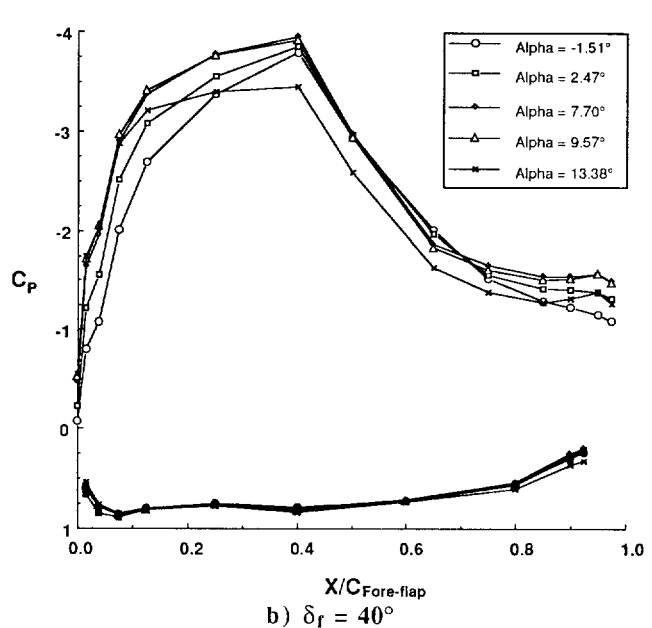


Figure 11. Concluded.

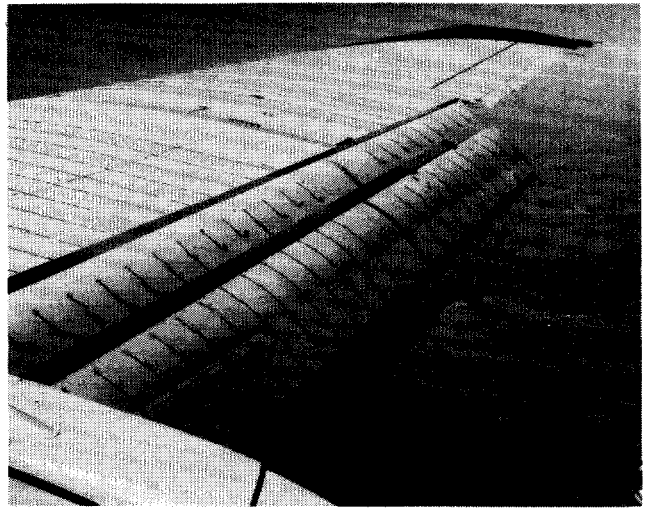


Figure 12. In-flight tuft-flow visualization.  $\delta_f = 40^\circ$ ,  $\alpha \approx 7^\circ$ .

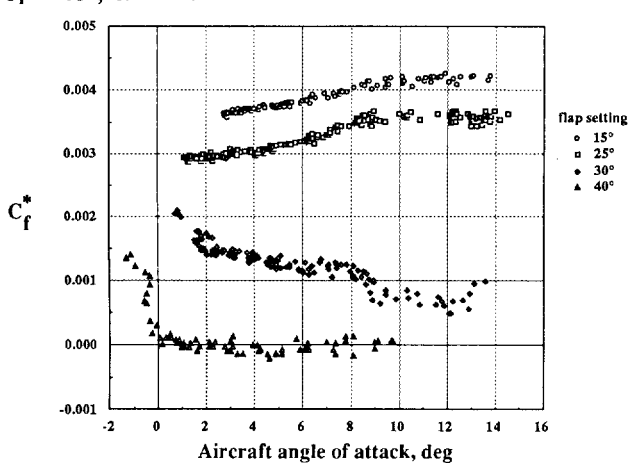


Figure 13. Fore-flap trailing-edge Preston-tube measurements. h = 5,000 ft. (from reference 3)

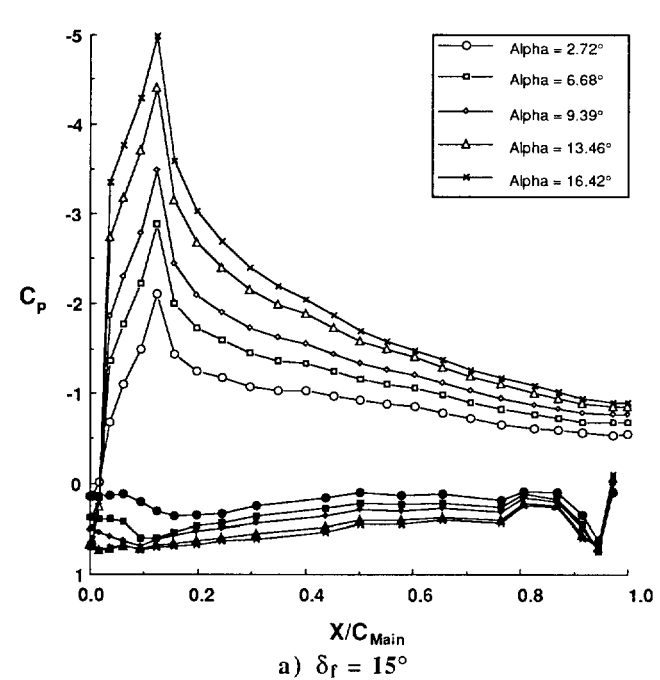
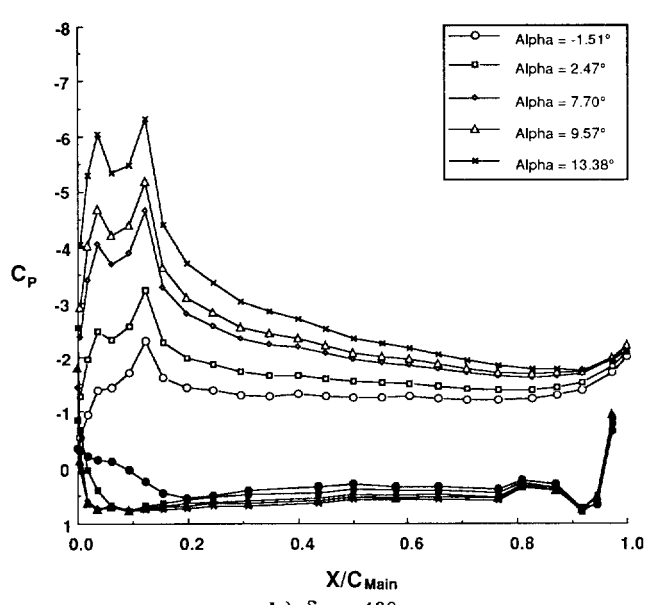


Figure 14. Measured main-element pressure distributions.



 $b) \ \delta_f = 40^{\circ}$  Figure 14. Concluded.

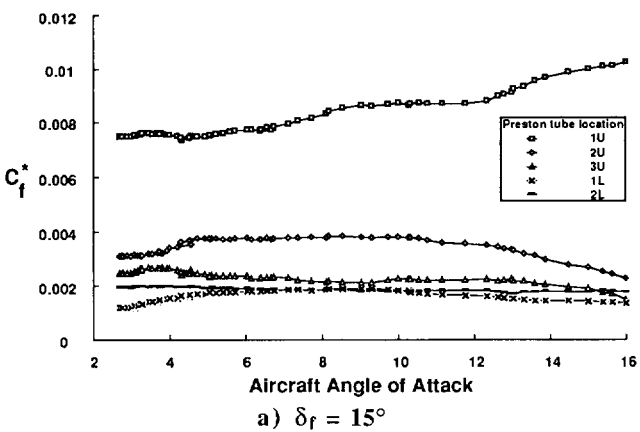


Figure 15. Main-element Preston-tube measurements. h = 10,000 ft.

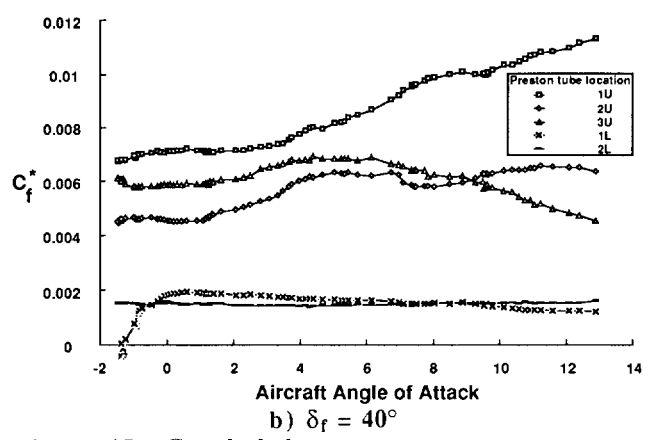


Figure 15. Concluded.

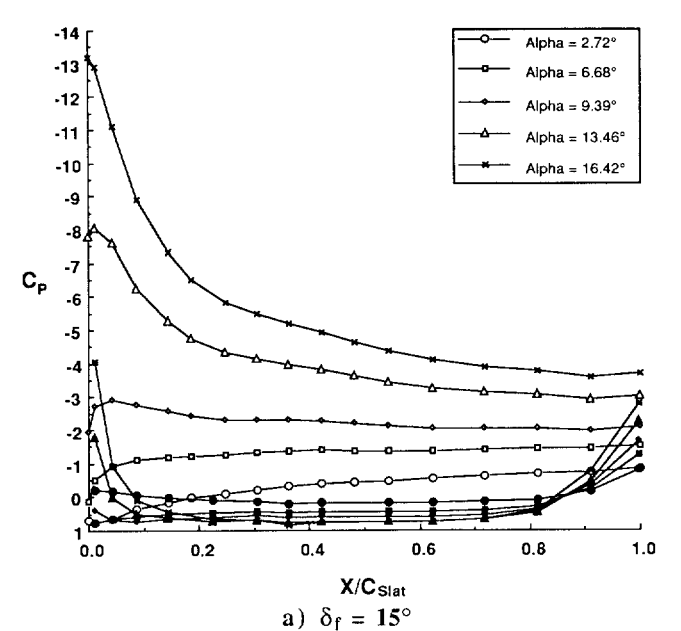


Figure 16. Measured slat pressure distributions.

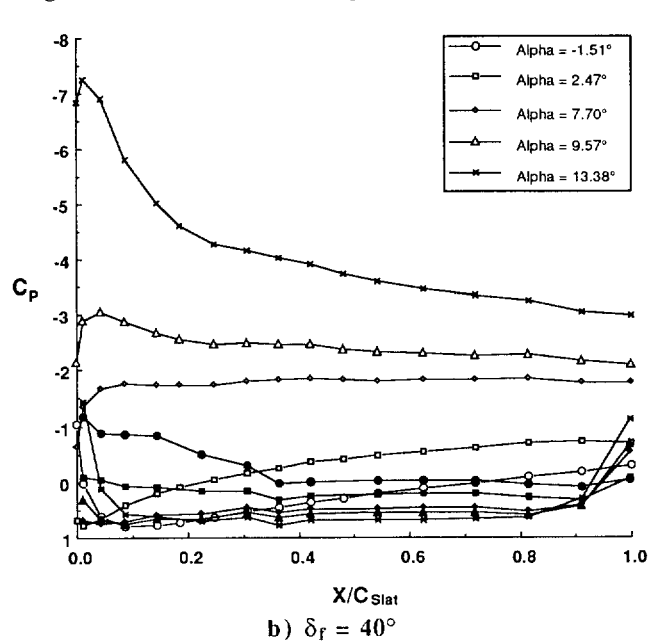


Figure 16. Concluded.

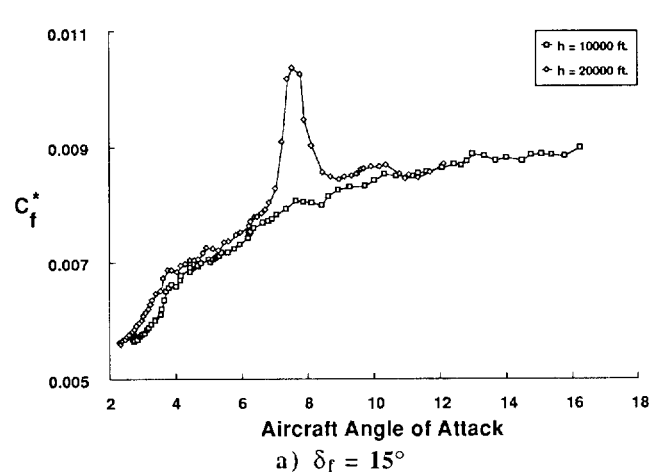


Figure 17. Slat Preston-tube measurements.

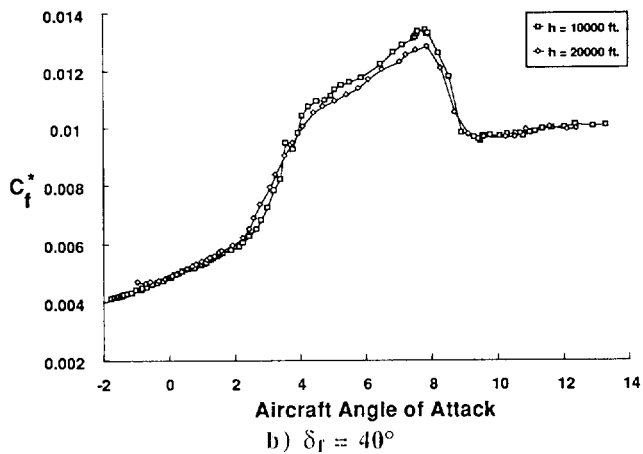


Figure 17. Concluded.

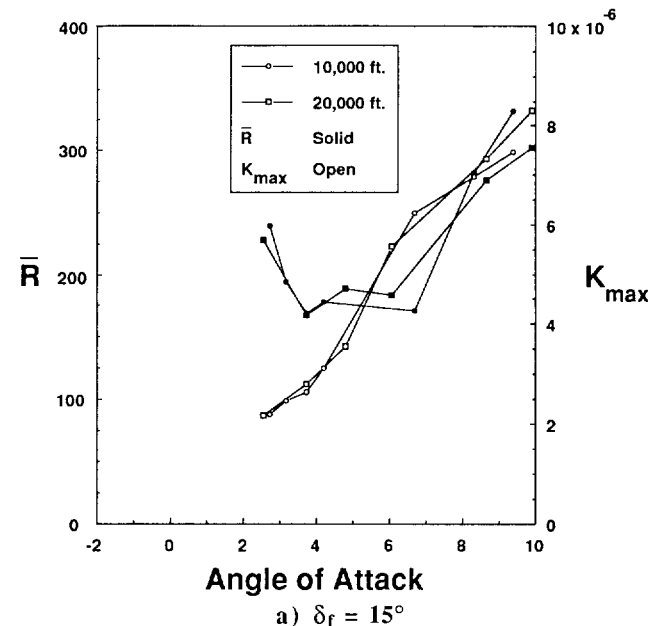
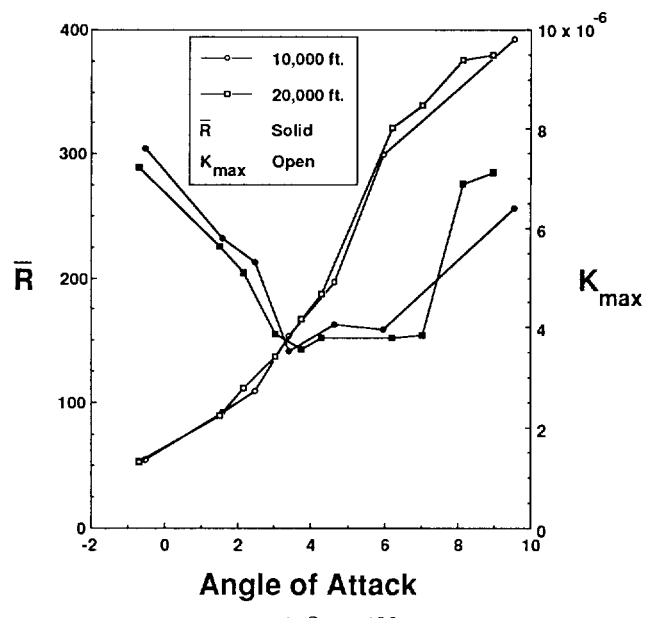


Figure 18. Attachment-line Reynolds number and relaminarization parameter for slat upper surface.



b)  $\delta_f$  = 40° Figure 18. Concluded.

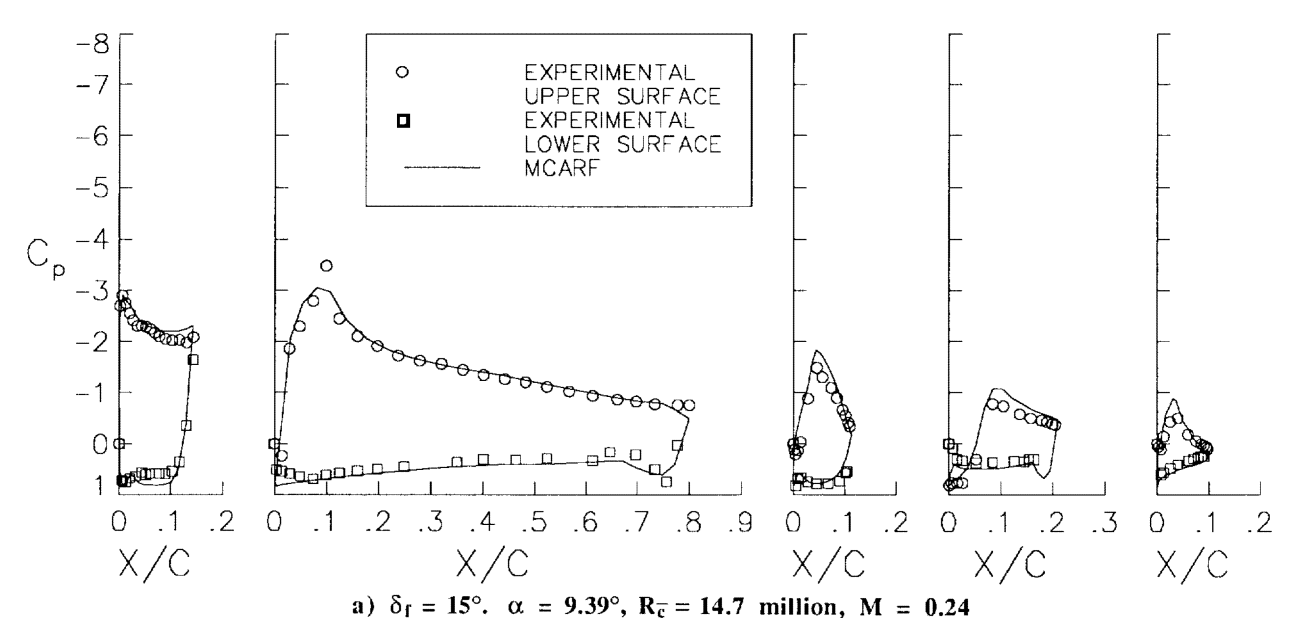


Figure 19. Comparison of MCARF and measured pressure distributions.

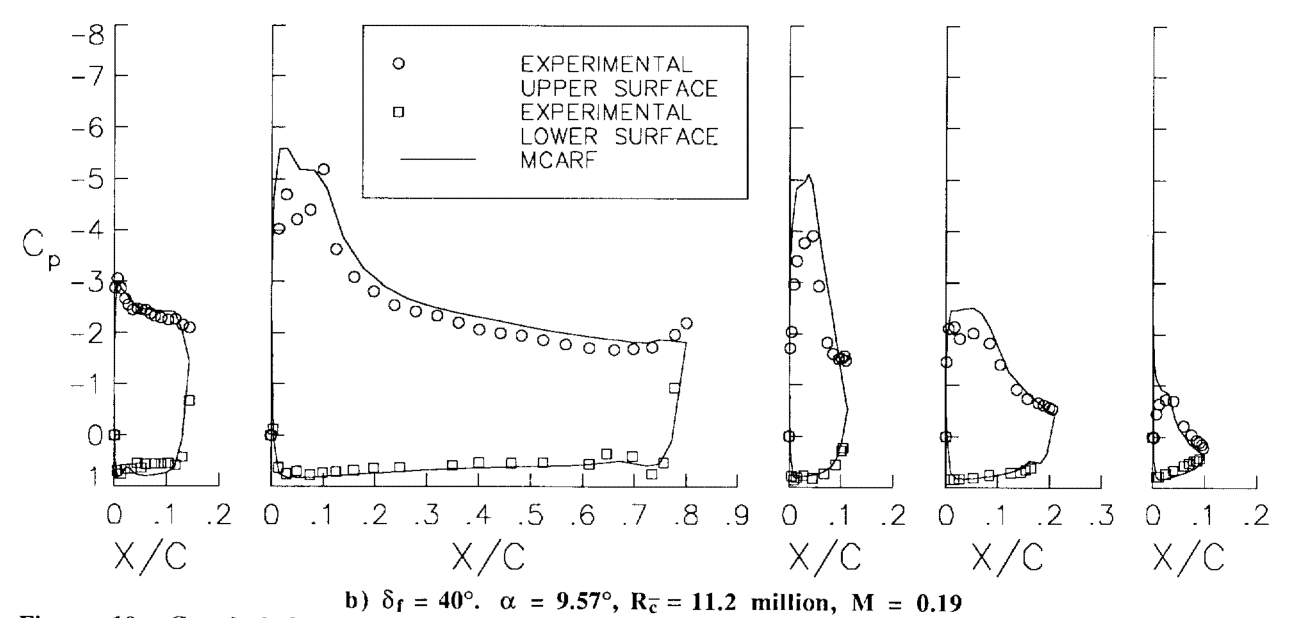


Figure 19. Concluded.

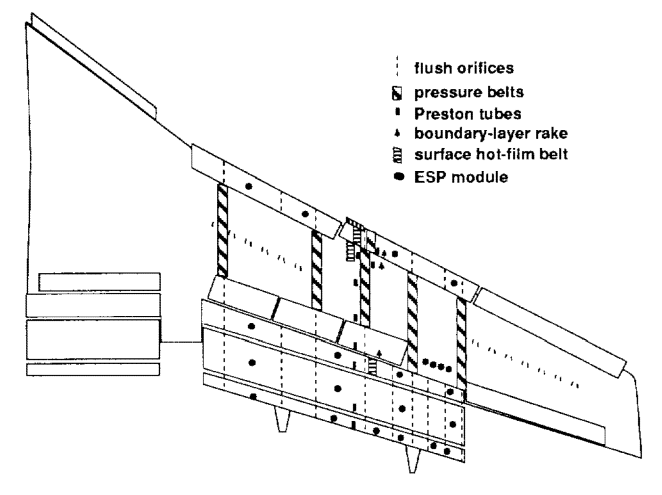


Figure 20. Instrumentation plans for future flight experiments.